

Two-photon double-beam optical bistability in the dispersive regime

P. Grangier, J. F. Roch, and J. Roger

Institut d'Optique, Boîte Postale 147, F-91406 Orsay CEDEX, France

L. A. Lugiato, E. M. Pessina, and G. Scandroglio

Dipartimento di Fisica dell'Università, via Celoria 16, 20133 Milano, Italy

P. Galatola

Dipartimento di Fisica del Politecnico, corso Duca degli Abruzzi 24, 10129 Torino, Italy

(Received 5 February 1992)

We report the observation and theoretical interpretation of two-photon double-beam optical bistability, where the nonlinearity is obtained in a two-photon transition in a sodium atomic beam. The experimental results, obtained in the dispersive regime, are compared with a simple crossed-phase-modulation model, and also with a numerical solution of the interaction between the cavity fields and three-level atoms, using the optical Bloch equations. For a wide range of parameters, both models agree with the experimental results. Oscillatory regimes may also appear, in agreement with the predictions of the complete model.

PACS number(s): 42.65.Pc, 42.50.—p

I. INTRODUCTION

Optical bistability (OB) has been the subject of continuous attention for many years [1]. Since the beginning of this interest, the intrinsic nonlinear character of the two-photon transition was thought to provide a convenient framework with which to obtain bistable behavior [2]. Two-photon OB, either in its absorptive part or in its dispersive part, has been theoretically studied [3–6] and experimentally observed, first by using a three-level atomic cascade [7], and also in solids [8,9]. All these experiments were performed in the degenerate case, where the nonlinearity acts on one mode of the electromagnetic field. The possibility of achieving multistable transmission characteristics by the interaction of two different modes of the field in a resonator filled with a two-photon nonlinear medium was also analyzed [10].

Also interesting is the dynamical behavior of optically bistable systems that utilize a two-photon transition. This problem has been analyzed in the degenerate case [11] by using an effective two-level model [12,13]. This model is obtained from the complete three-level description [14] by eliminating the variables of the intermediate level, under the condition of large detuning between the one-photon transition and the field frequency. The analysis of Ref. [11] reveals the presence of an instability that leads to the onset of spontaneous undamped oscillations in the output intensity. This instability, which becomes most invasive in the bad cavity limit (i.e., when the cavity damping rate is much larger than the atomic relaxation rates) belongs to a class of instabilities that is universal for systems displaying two-photon processes [15].

We recently considered the case of an atomic three-level system excited by two different laser beams [16,17]

with frequencies $\omega_0^{(1)}$ and $\omega_0^{(2)}$ close to the atomic resonances. For a certain range of parameters (which we call the dispersive $\chi^{(3)}$ limit), the basic physics of the nonlinear coupling can be understood very simply as a crossed-phase modulation effect: the refractive index for one beam is proportional to the intensity of the other beam. When this coupling is reinforced by the feedback of a cavity, bistable behavior, bifurcations and oscillations phenomena may appear.

In this paper we report the experimental observation of two-photon bistability under nondegenerate conditions, i.e., with a double-beam configuration. Under appropriate conditions, spontaneous oscillation in the output intensities of the two beams are also observed. We compare the experimental data with the theoretical predictions obtained from the complete three-level model, and also from a much simpler model obtained in the dispersive $\chi^{(3)}$ limit. In Sec. II we describe the experimental results, in Sec. III we discuss the complete, three-level semiclassical model, and in Sec. IV we discuss the latter's $\chi^{(3)}$ cubic approximation in the steady state. Section V is devoted to the illustration of the numerical results and to their comparison with the experimental data. The conclusions of this work are given in Sec. VI.

II. EXPERIMENTAL RESULTS

The experimental setup is shown in Fig. 1. The levels involved consist of the $3s_{1/2}$ - $3p_{3/2}$ - $3d_{5/2}$ atomic cascade in sodium. Two light beams at the required wavelengths of 589.0 (beam 1, yellow) and 819.5 nm (beam 2, infrared) are obtained from two cw, electronically stabilized dye lasers, pumped by a single argon-ion laser. A sodium atomic beam provides a density of 5×10^{11} atoms/cm³, with a Doppler width of about 200 MHz full width at

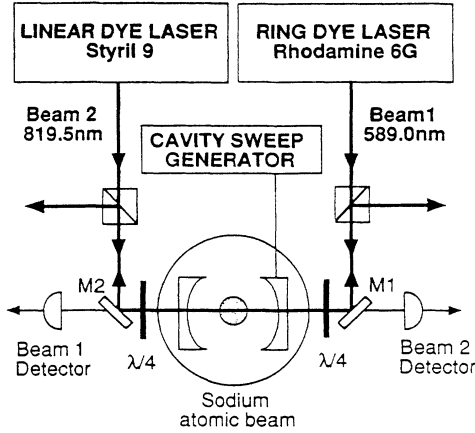


FIG. 1. Experimental setup. Two lasers at 589 and 819.5 nm are tuned close to resonances of the $3s_{1/2}-3p_{3/2}-3d_{5/2}$ cascade in a sodium atomic beam. The cavity resonates for each beam and is single-ended. The intracavity intensities are monitored through the dichroic mirrors M1 and M2.

half maximum (FWHM). The atomic beam is surrounded by a linear optical cavity (5.5 cm long, 5-cm mirror radius). The two laser beams are mode-matched to the cavity so that they resonate with only the corresponding longitudinal fundamental mode. Mirror M1 (M2) nearly totally reflects the infrared (yellow) beam. The transmit-

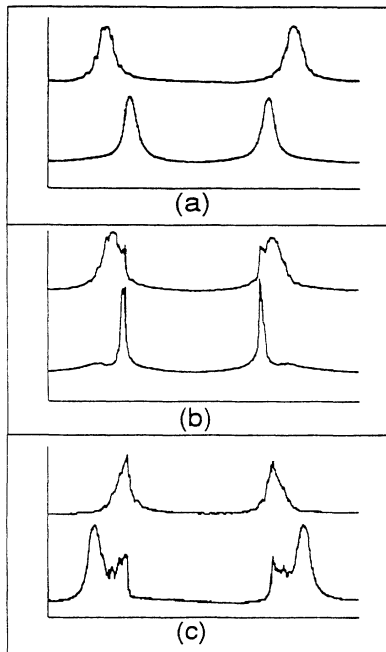


FIG. 2. Experimental observation of two-photon double-beam optical bistability. The lower curves are the resonances of the 589-nm beam and the upper curves those of the 819.5-nm beam, when the cavity length is swept back and forth. Curves labeled (a) represent the separate resonances (other beam turned off): the relative widths of the curves are due to the wavelengths difference between the two fields. Curves (b) and (c) are taken when both beams can resonate approximately for the same cavity length.

tivities of the input and output mirrors for both beams are $T_1 = T_2 = 0.025$, while the total losses (including the mirror transmittivity) are $P_1 = P_2 = 0.03$. The cavity width for each mode is therefore about 15 MHz FWHM. The light beams inside the cavity are circularly polarized in order to optimize the nonlinear coupling, and the output beams, reflected by the cavity, are separated from the input beams using prism polarizers. This configuration also reduces optical feedback inside the dye lasers. The cavity resonances for each mode of the field are observed through the small losses of the corresponding high-reflecting mirror.

Sodium is, of course, not a pure three-state system, and its real structure should be taken into account. However, for one-photon detunings (usually of the order of 10 GHz) much larger than the width $\Delta F = 1.8$ GHz between the two hyperfine sublevels of the fundamental $3s_{1/2}$, we

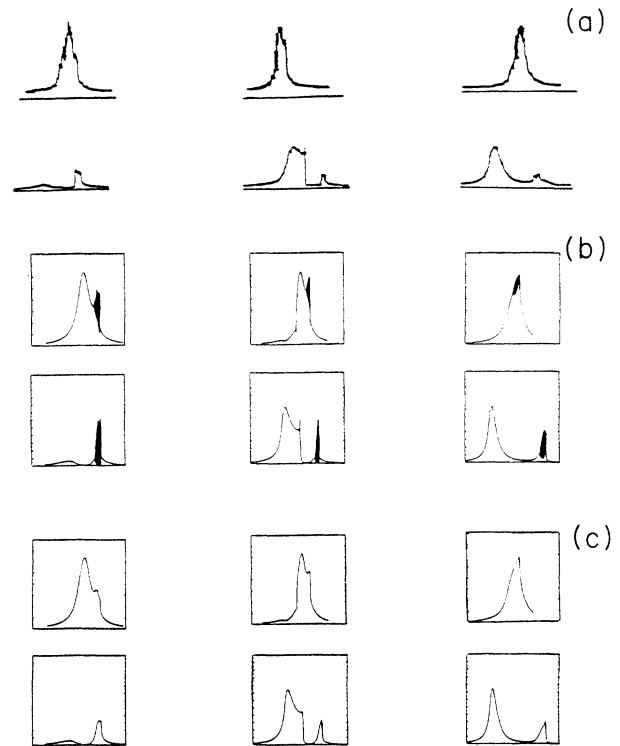


FIG. 3. Each column refers to a different case. All the parts of the figure are in pairs; the upper (lower) curve corresponds to the ir (yellow) field. Figures labeled (a) exhibit experimental traces obtained by a backward sweep of the cavity length for a higher ir input power ($\Omega_1^{\text{in}} = 46$ and $\Omega_2^{\text{in}} = 108$; see Sec. III). Figures labeled (b) show the intracavity intensities $|x_1|^2$ and $|x_2|^2$ as a result of the numerical solution of the complete three-level model obtained by a slow backward sweep of the cavity length. The dark regions correspond to the domains of spontaneous oscillation in the field intensities. The parameters are $C_1 = 31\,300$, $C_2 = 19\,540$, and $\Delta = 2400$, $\delta = 400$, $\gamma_1 = 30$ rad/s, and $\gamma_2/\gamma_1 = 0.83$. The initial values for the cavity-detuning parameters θ_1 and θ_2 used in the sweep are $\theta_1^0 = 2C_1/\Delta$ and $\theta_2^0 = 1.7$, 2.7, and 4.7 for left-hand, middle, and right-hand figures, respectively. The figures labeled (c) correspond to the curves of Figs. 1(b), 2(b), and 3(b), respectively, after averaging over the spontaneous oscillations.

can just consider the fine structure of the levels involved in the transition. In the $\sigma+\sigma+$ light-beam configuration, the interaction between the states $|3s\ J=\frac{1}{2},\ M=\frac{1}{2}\rangle$, $|3p\ J=\frac{3}{2},\ M=\frac{3}{2}\rangle$, and $|3d\ J=\frac{5}{2},\ M=\frac{5}{2}\rangle$ is by far the most intense. Since the other couplings can be neglected, we have a nearly closed, three-state system.

Typical results are reproduced in Fig. 2. In each part of the figure, and also in Figs. 3 and 5–8, the upper (lower) trace refers to the infrared (yellow) beam. The curves are obtained by sweeping the cavity length forward (left-hand part) and backward (right-hand part). Curves labeled (a) show the separate resonances of the two fields when the other field is turned off. Near the one-photon resonance between the $3s_{1/2}$ – $3p_{3/2}$ levels, the Fabry-Pérot curve of the 589-nm beam can become multivalued (one-photon bistability). By increasing the one-photon detuning, this behavior disappears and the cavity resonance is then just shifted due to linear dispersion. Curves (b) and (c) are then obtained when the two beams resonate approximately simultaneously in the cavity. The bistable behavior is obviously mixed with a switching phenomenon, and the observed curves depend both on the respective resonance positions and on the intensity ratio. As we will see, this is clearly a signature of the crossed-phase modulation effect.

When the intensity of the infrared (ir) beam is increased, the traces become more irregular [see Figs. 3(a), which exhibit the result of a backward sweep of the cavity length]. As we will discuss in the following sections, this feature is due to the emergence of spontaneous undamped oscillations in the intensities of the two fields. These oscillations are averaged out by the detectors in Fig. 3, but have been observed directly using faster detectors, under conditions of fixed cavity length.

III. THEORETICAL MODEL

The scheme of the energy levels is shown in Fig. 4. The parameters γ_1 and γ_2 denote one-half of the transition rates of the atomic population from the intermediate level, 2, to the lowest level, 1; and from the highest level, 3, to the intermediate level, 2, respectively. The observables of the single atom correspond to 3×3 matrices. In particular, the coherences between levels 1 and 2, 2 and 3, and 1 and 3 correspond, respectively, to the lowering operators

$$\begin{aligned} r^- &= \begin{pmatrix} 0 & 0 & 0 \\ 0 & 0 & 0 \\ 0 & 1 & 0 \end{pmatrix}, \\ s^- &= \begin{pmatrix} 0 & 0 & 0 \\ 1 & 0 & 0 \\ 0 & 0 & 0 \end{pmatrix}, \\ t^- &= \begin{pmatrix} 0 & 0 & 0 \\ 0 & 0 & 0 \\ 1 & 0 & 0 \end{pmatrix}, \end{aligned} \quad (1)$$

and to the corresponding adjoints (raising operators), r^+, s^+, t^+ . Similarly, the projection operators onto levels 1, 2, and 3 correspond, respectively, to the operators

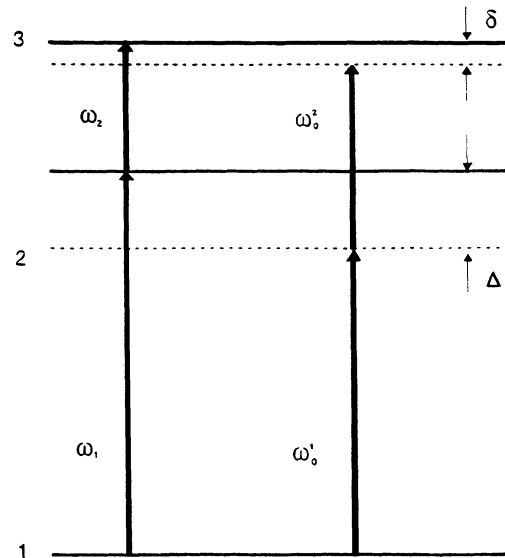


FIG. 4. Energy-level scheme.

$$\begin{aligned} P_1 &= \begin{pmatrix} 0 & 0 & 0 \\ 0 & 0 & 0 \\ 0 & 0 & 1 \end{pmatrix}, \\ P_2 &= \begin{pmatrix} 0 & 0 & 0 \\ 0 & 1 & 0 \\ 0 & 0 & 0 \end{pmatrix}, \\ P_3 &= \begin{pmatrix} 1 & 0 & 0 \\ 0 & 0 & 0 \\ 0 & 0 & 0 \end{pmatrix}. \end{aligned} \quad (2)$$

If we indicate by ρ the density matrix of the atom and assume that the electromagnetic field is in the vacuum state, the time evolution of ρ is governed by the master equation:

$$\frac{d\rho}{dt} = -\frac{i}{\hbar} [H_A, \rho] + \Lambda_A \rho, \quad (3)$$

where H_A is the Hamiltonian of the free atom,

$$H_A = \sum_{i=1}^3 E_i P_i, \quad (4)$$

and E_i ($i=1,2,3$) are the energies of the three levels. The Liouvillian Λ_A accounts for the relaxation processes of the atom and is given by

$$\begin{aligned} \Lambda_A \rho &= \gamma_1 ([r^-, \rho] + [r^-, \rho] r^+) \\ &\quad + \gamma_2 ([s^-, \rho] + [s^-, \rho] s^+) \\ &\quad + \sum_{i=1}^3 \eta_i ([P_i \rho, P_i] + [P_i, \rho P_i]), \end{aligned} \quad (5)$$

where the last term describes dephasing processes which arise from elastic collisions. Hence the polarization variables $r^-, s^-,$ and t^- have damping rates $\gamma_{1v}, \gamma_{1w},$ and γ_{1z} respectively, where

$$\begin{aligned} \gamma_{\perp v} &= \gamma_1 + \eta_1 + \eta_2, \\ \gamma_{\perp w} &= \gamma_1 + \gamma_2 + \eta_2 + \eta_3, \\ \gamma_{\perp z} &= \gamma_2 + \eta_1 + \eta_3. \end{aligned} \quad (6)$$

On the other hand, the two population-inversion variables

$$r_3 = \frac{1}{2} \begin{pmatrix} 0 & 0 & 0 \\ 0 & 1 & 0 \\ 0 & 0 & -1 \end{pmatrix}, \quad s_3 = \frac{1}{2} \begin{pmatrix} 1 & 0 & 0 \\ 0 & -1 & 0 \\ 0 & 0 & 0 \end{pmatrix} \quad (7)$$

have relaxation rates

$$\gamma_{\parallel m} = 2\gamma_1 \quad \text{and} \quad \gamma_{\parallel n} = 2\gamma_2, \quad (8)$$

respectively. We call ω_1 (ω_2) the Bohr transition frequency between levels 1 and 2 (2 and 3), and we designate by $\omega_0^{(1)}$ ($\omega_0^{(2)}$) the frequency of the driving field which is close to resonance with the transition $1 \leftrightarrow 2$ ($2 \leftrightarrow 3$). The one-photon atomic detuning parameter is given by (see Fig. 4)

$$\Delta = \omega_1 - \omega_0^{(1)}; \quad (9)$$

the two-photon atomic detuning parameter is defined as

$$\delta = \omega_1 + \omega_2 - (\omega_0^{(1)} + \omega_0^{(2)}). \quad (10)$$

We assume, on the other hand, that the input frequencies $\omega_0^{(1)}$ and $\omega_0^{(2)}$ are close to resonance with two cavity frequencies $\omega_c^{(1)}$ and $\omega_c^{(2)}$, respectively, and we define two cavity detuning parameters θ_1 and θ_2 as follows:

$$\theta_i = \frac{\omega_c^{(i)} - \omega_0^{(i)}}{k_i}, \quad i=1,2 \quad (11)$$

where k_i ($i=1,2$) are the loss parameters for the two modes, namely

$$k_i = \frac{cP_i}{2\mathcal{L}}, \quad i=1,2 \quad (12)$$

\mathcal{L} being the round-trip cavity length. The factor 2 in the denominator arises from the fact that each of the two mirrors M1 and M2 (Fig. 1) is nearly totally reflecting for one of the two beams. In the following, for the sake of simplicity, we neglect standing-wave effects and we simulate the system using a ring cavity model with a total length equal to twice the length of the linear cavity used in the experiment.

It is convenient to formulate the semiclassical model in terms of normalized variables. We introduce the following quantities.

(a) Cavity-mode amplitudes

$$x_1 = \frac{\mu_1 E_1}{\hbar(\gamma_{\perp v} \gamma_{\parallel m})^{1/2}}, \quad x_2 = \frac{\mu_2 E_2}{\hbar(\gamma_{\perp v} \gamma_{\parallel m})^{1/2}}, \quad (13)$$

where E_1 and E_2 are the slowly varying envelopes of the two intracavity fields, and μ_1 (μ_2) is the modulus of the dipole moment of the atomic transition $1 \leftrightarrow 2$ ($2 \leftrightarrow 3$).

(b) Input field variables

$$\begin{aligned} y_1 &= \frac{2(T_1)^{1/2}}{P_1} \frac{\mu_1 E_1^{\text{in}}}{\hbar(\gamma_{\perp v} \gamma_{\parallel m})^{1/2}}, \\ y_2 &= \frac{2(T_2)^{1/2}}{P_2} \frac{\mu_2 E_2^{\text{in}}}{\hbar(\gamma_{\perp v} \gamma_{\parallel m})^{1/2}}, \end{aligned} \quad (14)$$

where E_1^{in} and E_2^{in} denote the amplitudes of the two input fields.

(c) Atomic polarizations

$$\begin{aligned} v &= -2 \left[\frac{\gamma_{\perp v}}{\gamma_{\parallel m}} \right]^{1/2} \langle r^- \rangle, \\ w &= -2 \left[\frac{\gamma_{\perp v}}{\gamma_{\parallel m}} \right]^{1/2} \langle s^- \rangle, \\ z &= -\langle t^- \rangle \end{aligned} \quad (15)$$

where N is the number of atoms.

(d) Population inversions

$$m = -\frac{2}{N} \langle r_3 \rangle, \quad n = -\frac{2}{N} \langle s_3 \rangle. \quad (16)$$

In terms of these variables the semiclassical equations read

$$\dot{x}_1 = k_1 [-(1+i\theta_1)x_1 + y_1 - 2C_1 v], \quad (17a)$$

$$\dot{x}_2 = k_2 [-(1+i\theta_2)x_2 + y_2 - 2C_2 w], \quad (17b)$$

$$\dot{v} = \gamma_{\perp v} [-(1+i\bar{\Delta})v + x_1 m + x_2^* z], \quad (17c)$$

$$\dot{w} = \gamma_{\perp v} \left[-\left[\frac{\gamma_{\perp w}}{\gamma_{\perp v}} + i(\bar{\delta} - \bar{\Delta}) \right] w + x_2 n - x_1^* z \right], \quad (17d)$$

$$\dot{z} = \gamma_{\perp z} \left[-\left[1 + i \frac{\gamma_{\perp v}}{\gamma_{\perp z}} \bar{\delta} \right] z + \frac{\gamma_{\parallel m}}{4\gamma_{\perp z}} w x_1 - \frac{\gamma_{\parallel m}}{4\gamma_{\perp z}} v x_2 \right], \quad (17e)$$

$$\begin{aligned} \dot{m} &= \gamma_{\parallel m} \left[\frac{1}{3} (\xi - 2)(m - 1) + \frac{2}{3} (1 + \xi)n \right. \\ &\quad \left. - \frac{1}{2} (x_1^* v + x_1 v^*) + \frac{1}{4} (x_2^* w + x_2 w^*) \right], \end{aligned} \quad (17f)$$

$$\begin{aligned} \dot{n} &= \gamma_{\parallel n} \left[\frac{1}{3} \left[\frac{1}{\xi} - 2 \right] (m - 1) - \frac{1}{3} \left[\frac{1}{\xi} + 4 \right] n \right. \\ &\quad \left. - \frac{1}{2\xi} (x_2^* w + x_2 w^*) + \frac{1}{4\xi} (x_1^* v + x_1 v^*) \right], \end{aligned} \quad (17g)$$

where $\bar{\Delta}$ and $\bar{\delta}$ denote the atomic detuning parameters Δ and δ , respectively, normalized to $\gamma_{\perp v}$; we set

$$\xi = \frac{\gamma_{\parallel n}}{\gamma_{\parallel m}}, \quad (18)$$

and the bistability parameters C_1 and C_2 are defined as follows:

$$C_1 = \frac{\alpha^{\text{field}} l}{P_1}, \quad C_2 = \left[\frac{\mu_2}{\mu_1} \right]^2 \frac{\omega_2}{\omega_1} \frac{\alpha^{\text{field}} l}{P_2}, \quad (19)$$

l being the length of the atomic sample and α^{field} the ab-

sorption coefficient per unit length for the lower transition $1 \leftrightarrow 2$. We also have

$$\alpha^{\text{field}} = \frac{3}{4\pi} n_{\text{at}} \lambda_1^2, \quad \lambda_1 = \frac{2\pi c}{\omega_1}. \quad (20)$$

In Eq. (20), n_{at} denotes the atomic density. In writing the expression of C_1 , we have taken into account that each of the two mirrors M1 and M2 (Fig. 1) is nearly completely reflecting for one of the two beams; the same consideration holds for the definition (14) of y_1 and y_2 .

The model (17) holds in the uniform field limit [1(b)] and in the plane-wave approximation. We neglect the Doppler effect of the atomic velocity distribution since all atomic detunings are much larger than the Doppler width.

IV. THE $\chi^{(3)}$ APPROXIMATION

In the limit of large atomic detunings

$$\bar{\Delta}, \bar{\delta} \gg 1, \quad |x_1|, |x_2|, \quad (21)$$

the steady-state equations for our model can be written in a very simplified form which allows for a straightforward physical interpretation in terms of $\chi^{(3)}$ processes. As a matter of fact, in the limit Eq. (21) one can introduce expansions in power of the electric fields and keep, in the final field equations, terms up to third order (cubic approximation). Precisely, the steady-state equations obtained in this limit read

$$x_1 = \frac{y_1}{1 + i \left[\theta_1 - 2C_1 \left(\frac{1}{\bar{\Delta}} - \frac{|x_1|^2}{\bar{\Delta}^3} + \frac{\gamma_{\parallel m} |x_2|^2}{4\gamma_{\perp v} \bar{\Delta}^2 \bar{\delta}} \right) \right]}, \quad (22)$$

$$x_2 = \frac{y_2}{1 + i \left[\theta_2 - 2C_2 \frac{\left[2 \frac{\gamma_{\perp v} \bar{\delta} - \bar{\Delta}}{\gamma_{\parallel m}} \right] \gamma_{\parallel m}}{4\gamma_{\perp v} \bar{\Delta}^2 \bar{\delta} (\bar{\delta} - \bar{\Delta})} |x_1|^2 \right]}.$$

In the case of purely radiative damping ($\eta_i = 0$, $\gamma_{\perp v} = \gamma_{\perp m} / 2 = \gamma_1$), Eqs. (22) take the simpler form

$$x_1 = \frac{y_1}{1 + i \left[\theta_1 - 2C_1 \left(\frac{1}{\bar{\Delta}} - \frac{|x_1|^2}{\bar{\Delta}^3} + \frac{|x_2|^2}{2\bar{\Delta}^2 \bar{\delta}} \right) \right]}, \quad (22')$$

$$x_2 = \frac{y_2}{1 + i \left[\theta_2 - 2C_2 \frac{|x_1|^2}{2\bar{\Delta}^2 \bar{\delta}} \right]}.$$

The different terms in these two equations have clear signification: $2C_1/\bar{\Delta}$ is just a linear phase shift due to the one-photon resonance (which can be reincluded in θ_1), $2C_1|x_1|^2/\bar{\Delta}^3$ is the nonlinear dispersion due to the saturation of the same one-photon transition (and responsible for one-photon dispersive bistability), while $C_1|x_2|^2/(\bar{\Delta}^2\bar{\delta})$ and $C_2|x_1|^2/(\bar{\Delta}^2\bar{\delta})$ represent the nonlinear two-photon dispersion described above (cross-phase modulation). These two terms can be interpreted

as nonlinear phase shifts Φ_1^{nl} and Φ_2^{nl} normalized to $P_1/2$ and $P_2/2$, respectively:

$$\Phi_1^{\text{nl}} = \alpha_0^{\text{field}} \frac{l}{4} \frac{\mu_2^2 \gamma_1}{\hbar^2 \Delta^2 \bar{\delta}} |E_2|^2, \quad (23a)$$

$$\Phi_2^{\text{nl}} = \alpha_0^{\text{field}} \frac{l}{4} \frac{\omega_2}{\omega_1} \frac{\mu_2^2 \gamma_1}{\hbar^2 \Delta^2 \bar{\delta}} |E_1|^2. \quad (23b)$$

By using the usual definition of the transverse linewidth,

$$\gamma_1 = \frac{1}{6\pi\epsilon_0} \frac{\omega_1^3}{\hbar c^3} \mu_1^2, \quad (24)$$

one can obtain more symmetrical forms for these two phase-shifts:

$$\Phi_1^{\text{nl}} = n_{\text{at}} \frac{l}{8} \frac{\omega_1 \omega_2 \mu_1^2 \mu_2^2}{\epsilon_0 \hbar^2 c \Delta^2 \bar{\delta}} \frac{|E_2|^2}{\hbar \omega_2}, \quad (25a)$$

$$\Phi_2^{\text{nl}} = n_{\text{at}} \frac{l}{8} \frac{\omega_1 \omega_2 \mu_1^2 \mu_2^2}{\epsilon_0 \hbar^2 c \Delta^2 \bar{\delta}} \frac{|E_1|^2}{\hbar \omega_1}, \quad (25b)$$

which show us that they are equal if the field intensities are the same in photon units: this is a characteristic of a pure parametric effect, and can be directly derived by solving the optical Bloch equations for a three-level system [14]. Near the two-photon resonance and for $\Delta \gg \delta$, there is no one-photon bistability and this two-photon dispersive nonlinearity is the only relevant effect.

The effect of collisions can be best identified by using a slightly different definition for the field variables and the parameters, namely ($i=1,2$)

$$x'_i = v^{1/2} x_i, \quad y'_i = v^{1/2} y_i, \quad (26)$$

$$C'_i = v C_i, \quad \Delta' = v \bar{\Delta}, \quad \delta' = v \bar{\delta},$$

with

$$v = \gamma_{\perp v} / \gamma_1. \quad (27)$$

The new normalized parameters defined according to Eqs. (26) and (27) are independent of the collision rates, and Eqs. (22) take the form

$$y'_1 = x'_1 \left[1 + i \left[\theta_1 - \frac{2C'_1}{\Delta'} + \frac{2C'_1 |x'_1|^2}{(\Delta')^3} (1 + T_{\text{coll}}) - \frac{C'_1 |x'_2|^2}{(\Delta')^2 \delta'} \right] \right], \quad (28)$$

$$y'_2 = x'_2 \left[1 + i \left[\theta_2 - \frac{C'_2 |x'_1|^2}{(\Delta')^2 \delta'} \times \left[1 + T_{\text{coll}} \frac{\delta'}{(\delta' - \Delta')} \right] \right] \right],$$

where all effects of collisions are included in the parameter

$$T_{\text{coll}} = \frac{\eta_1 + \eta_2}{\gamma_1}. \quad (29)$$

When $\delta \ll \Delta$, it appears clearly that the collision-dependent terms are reduced by a factor (δ/Δ) (just like the self-phase modulation effect) relative to the cross-phase modulation effect. Therefore, the collisional contributions are negligible for $1/\delta \gg T_{\text{coll}}/\Delta$. This should be satisfied in our experiment. This result leads also to the interesting conclusion that the two-photon nonlinear effect (scaling as $1/\Delta^2\delta$) is less affected by collisions than the one-photon nonlinear effect in two-level atoms [scaling as $(1+T_{\text{coll}})/\Delta^3$].

One can easily verify that, in the limit $1/\delta \gg T_{\text{coll}}/\Delta$ in which self-phase modulation and collisional broadening are negligible, Eq. (22') can be written in a very compact form. In fact, by setting

$$\begin{aligned}\bar{x}_1 &= (C_2/\Delta^2|\delta|)^{1/2}x_1, & \bar{y}_1 &= (C_2/\Delta^2|\delta|)^{1/2}y_1, \\ \bar{x}_2 &= (C_1/\Delta^2|\delta|)^{1/2}x_2, & \bar{y}_2 &= (C_1/\Delta^2|\delta|)^{1/2}y_2, \\ \bar{\theta}_1 &= \theta_1 - \frac{2C_1}{\Delta}, & \bar{\theta}_2 &= \theta_2,\end{aligned}\quad (30)$$

Eqs. (22) and (22') reduce to

$$\bar{x}_1 = \frac{\bar{y}_1}{1+i(\bar{\theta}_1 \pm |\bar{x}_2|^2)}, \quad (31a)$$

$$\bar{x}_2 = \frac{\bar{y}_2}{1+i(\bar{\theta}_2 \pm |\bar{x}_1|^2)} \quad (31b)$$

and depend only on the four parameters $\bar{y}_1, \bar{y}_2, \bar{\theta}_1$ and $\bar{\theta}_2$. Equations (31) represent the generalization of the simple model of two-photon optical bistability given in Ref. [16]. In Eqs. (31) one must take the negative (positive) sign when δ is positive (negative).

It is important to note that, even if in the limit of large atomic detunings one can obtain a cubic model that describes the steady-state behavior of the system, the same is not true for the dynamical behavior. As a matter of fact, a cubic model for the time evolution of the systems holds only in the good cavity limit, k_1 and k_2 much less than the atomic relaxation rates, but this is not true in the case of our experiment. This cubic model predicts the onset of spontaneous oscillations, in qualitative agreement with the experimental observations, but the oscillation frequency is proportional to k_1 and k_2 , which differs from the experimental case.

For the same reason, one cannot perform a simple linear-stability analysis in the cubic approximation. In the conditions of our experiment, the linear-stability analysis must be done by linearizing the complete model (17) around steady state. The linear-stability analysis reveals, as usual, that the negative-slope parts of the steady-state curves of $|x_1|^2$ and $|x_2|^2$ (as a function, for example, of the input intensities or of the cavity length) are unstable. In addition, it is easy to meet situations in which some segments of the steady-state curves with positive slope are unstable. In this case, one has the onset of spontaneous oscillations in the output intensities. The presence of these oscillatory instabilities agrees very well with the predictions of the models of two-photon bistability based on the effective two-level description [11,15].

V. NUMERICAL RESULTS

In order to meet the conditions of the experiment—in which one performs a slow forward and backward sweep of the cavity length—in our numerical calculations, we sweep the cavity detuning parameters θ_1 and θ_2 of the two fields starting from initial values θ_1^0 and θ_2^0 and setting $\theta_1 = \theta_1^0 + \delta\theta$, $\theta_2 = \theta_2^0 + (\lambda_2/\lambda_1)\delta\theta$, where the factor λ_2/λ_1 takes into account that, upon variations of cavity length, the variation of θ_1 and θ_2 are in the ratio λ_2/λ_1 . Some of the curves we will show display the stationary solutions of Eqs. (17) [or the solution of Eqs. (22), if one considers the $\chi^{(3)}$ approximation] as a function of $\delta\theta$, whereas other curves are obtained by performing a slow forward or backward sweep of θ_1 and θ_2 , as described before, in the full dynamical equations (17) (i.e., including the derivatives with respect to time). The second type of curve can indicate the presence of oscillatory instabilities and display the location of the unstable domains. Because the experimental curves attained by sweeping the cavity length are obtained using a detector with a narrow frequency bandwidth that averages the oscillations in the output power of the two fields, we also consider curves derived by introducing an averaging of the oscillations in our numerical results. All the following data refer to the collisionless case $\eta_i = 0$ ($i = 1, 2, 3$).

Figure 5 shows the numerical solutions of the two coupled stationary equations (22) for a linear scan of the cavity length with different initial positions θ_1^0 and θ_2^0 of the two separate resonances. The bistability parameters are $C_1 = 31\,300$ and $C_2 = 1.6C_1$ for $\alpha^{\text{field}} = 940$ (taking into account the double pass in the atomic beam for our experimental linear cavity). The other parameters correspond to the values of the experiment shown in Fig. 2: the detunings are $\bar{\Delta} = 2400$ and $\bar{\delta} = 400$. The input Rabi frequencies, expressed in γ_1 units, are $\Omega_1^{\text{in}} = 48$ and $\Omega_2^{\text{in}} = 66$, so that $y_1 = 360$ and $y_2 = 490$. Note that we obtain strong nonlinear effects with very small laser intensities (typical powers of the order of 1 mW). One can clearly see a nonsymmetric behavior between $\theta_2^0 < \theta_1^0$

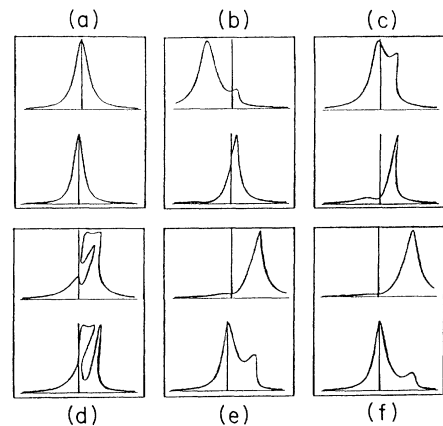


FIG. 5. Stationary solutions of the χ^3 model for different values of the initial detuning parameter θ_2^0 ($\theta_1^0 = 2C_1/\bar{\Delta}$). (a) $\theta_2^0 = 0$, (b) $\theta_2^0 = 0.7$, (c) $\theta_2^0 = 1.4$, (d) $\theta_2^0 = 2.1$ (e) $\theta_2^0 = 2.8$, and (f) $\theta_2^0 = 3.5$. The values of the other parameters are specified in the text.

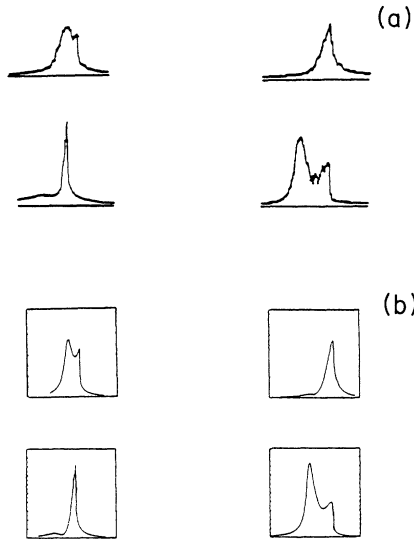


FIG. 6. Curves labeled (a), left and right, coincide with the experimental curves shown in Figs. 2(b) (backward sweep) and 2(c) (forward sweep), respectively. Graphs labeled (b) are obtained by a linear sweep of the cavity length in the complete three-level model; the values of the parameters are the same as in Figs. 5(c) and 5(e), respectively; in addition, $\gamma_1=30$ rad/s and $\gamma_2/\gamma_1=0.83$.

(where beam 2 switches beam 1 outside its cavity resonance) and $\theta_2^0 > \theta_1^0$ (where it is just the opposite). For equal input intensities, the switching limit occurs exactly at $\theta_2^{0\text{lim}} = \theta_1^0$, but for different intensities the most powerful beam tends to stay longer at resonance: e.g., if beam 2 is stronger than beam 1, then the switching limit is now at $\theta_2^{0\text{lim}} > \theta_1^0$.

In this range of values of the input intensities and atomic detuning parameters, the stationary solutions obtained from the complete model (17) differ very little from those given by the $\chi^{(3)}$ approximation. This can be seen, for example, in the four panels comprising Fig. 6(b), which corresponds to Figs. 5(c) and 5(e), respectively. The same figure shows also the comparison with the experimental curves in Figs. 2(b) and 2(c), which turns out to be satisfactory.

Figure 7 shows a case in which the slope of the steady-

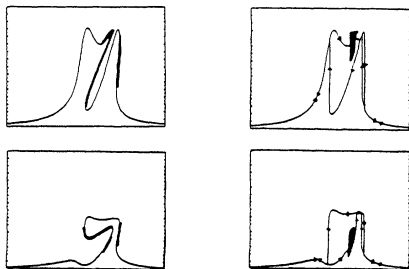


FIG. 7. The left-hand curves are the steady-state solutions of the complete three-level model. The thick segments correspond to unstable states. The right-hand curves are the result of a forward and backward sweep of $\delta\theta$. The parameters are $C_1=31\,300$, $C_2=27\,350$, $\Delta=2400$, $\delta=400$, $\gamma_1=30$ rad/s, and $\gamma_2/\gamma_1=0.83$.

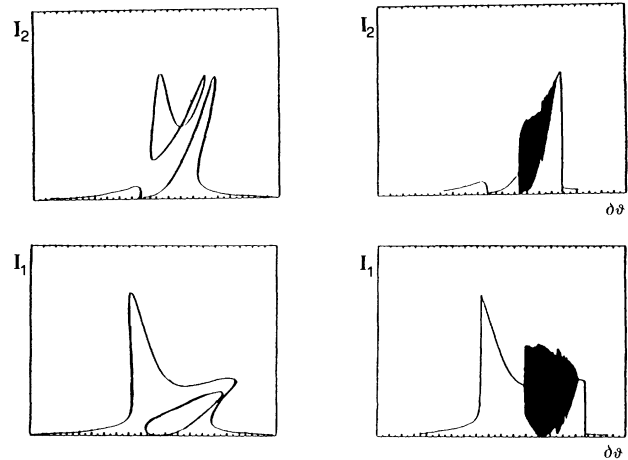


FIG. 8. The parameters are $C_1=31\,300$, $C_2=27\,350$, $\Delta=2400$, $\delta=400$, $\gamma_1=30$ rad/s, and $\gamma_2/\gamma_1=0.83$. The left-hand curves display the steady-state solutions of Eqs. (17), while those on the right are obtained by sweeping the parameter $\delta\theta$.

state curve leads to a double hysteresis cycle. In this case, there is an unstable positive-slope segment of the steady-state curve which leads to spontaneous oscillations. The presence of oscillations becomes commonplace if one increases the intensity of the ir beam to $\Omega_2^{\text{in}}=108$ as in Fig. 3 (keeping the other parameters unchanged with respect to Figs. 2, 5, and 6). As a matter of fact, the complete model predicts that extended parts of the steady-state curves become unstable and lead to the

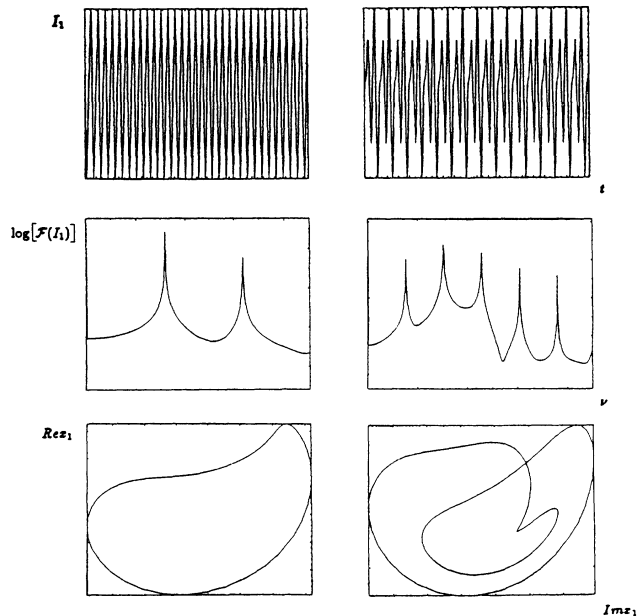


FIG. 9. Each column refers to a different value of the parameter $\delta\theta$. The values of the other parameters are the same as in Fig. 8. The upper curves show the intensity oscillations of field 1; the middle curves the corresponding spectrum (on a logarithmic scale), and the lower curves the projection of the phase-space trajectory onto the plane of the variables $(\text{Re}x_1, \text{Im}x_1)$. Left, $\delta\theta=3.01$; right, $\delta\theta=4.52$.

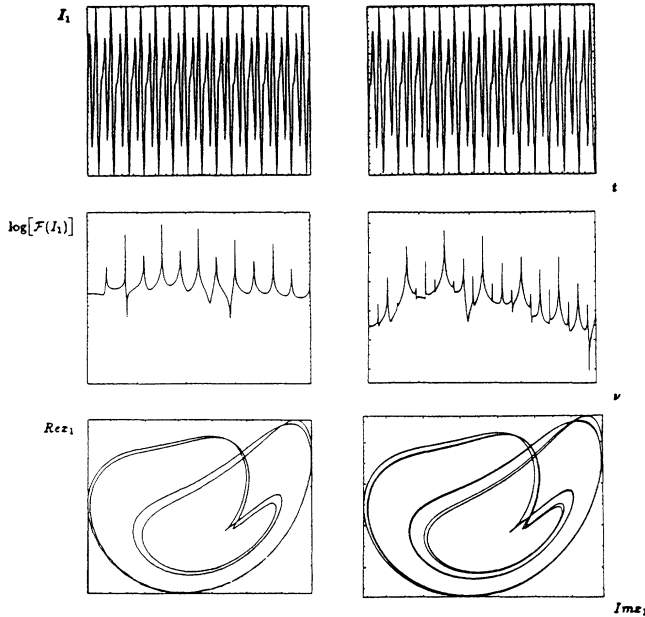


FIG. 10. Same as Fig. 9, but for left, $\delta\theta=4.61$, and right, $\delta\theta=4.64$.

onset of oscillations. The oscillation frequencies are calculated to be in the range 5–15 MHz, depending on the values of θ_1^0 and θ_2^0 , and change notably along the steady-state curve when one passes from one to the other extreme of the unstable positive-slope segment. The numerical values of the oscillation frequencies agree quite well with the values which are experimentally observed, using a fast detector and a spectrum analyzer. On the other hand, these oscillations are averaged out by the detectors

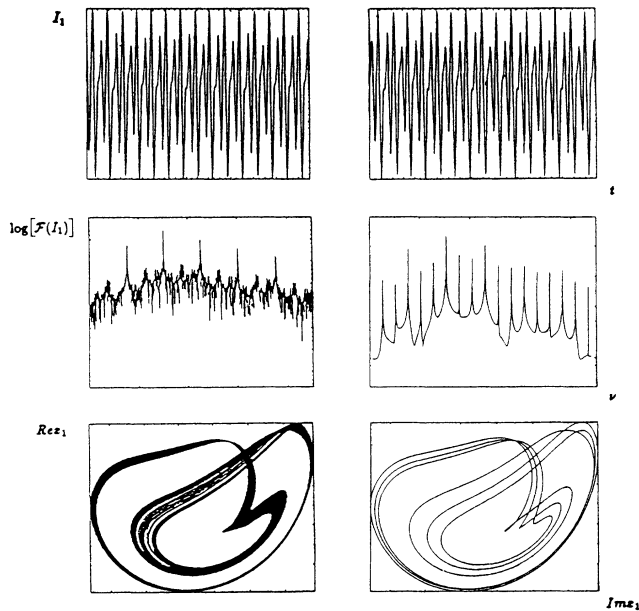


FIG. 11. Same as Fig. 9, but for left, $\delta\theta=4.68$, and right, $\delta\theta=4.70$.

on Figs. 2 and 3. A comparison with the experimental results is attempted in Fig. 3. The six panels comprising Fig. 3(b) show the curves obtained in a dynamical sweep of the complete three-level model, while the six panels of Fig. 3(c) show the result of averaging the oscillations out.

The character of the oscillations becomes complex when the input powers are increased. Let us consider, for example, Fig. 8, which shows both the steady-state curves, obtained from the complete model (17), and the corresponding dynamically swept curves. In this case the steady-state curves display the presence of an island, and the thick segments of the steady-state curves are unstable. By varying the cavity length (i.e., $\delta\theta$) one meets oscillations of period 1 [Fig. 9 (left)], period 2 [Fig. 9 (right)], period 4 [Fig. 10 (left)], and period 8 [Fig. 10 (right)]; the period-doubling sequence leads, as usual, to chaos [Fig. 11 (left)]. An example of the period-6 window in the chaotic domain is shown in Fig. 11 (right).

VI. CONCLUDING REMARKS

We have observed two-photon double-beam optical bistability, and we carried out a rather detailed comparison between experimental data and the theoretical description. We used both a complete three-level model and an appropriate $\chi^{(3)}$ approximation that holds in the limit of very large atomic detunings and describes the behavior of the system in terms of cross-phase modulation.

The comparison of theory and experiment is very satisfactory for sufficiently small values of the input intensities (see Fig. 6). For larger values of the input power of field 2, the agreement is still reasonably good in some cases [see, for instance, Fig. 3 (left and middle columns)], and much worse in other cases [Fig. 3 (right column)]. The main source of discrepancy may lie in the fact that the calculations use a plane-wave approximation in a ring geometry, whereas the experiment is done in a linear cavity with Gaussian beams. It is very satisfactory that the experiment really reveals the presence of spontaneous oscillations in the output intensities where theory predicts them, and with the same frequency.

It has been shown that one-photon optical bistability can subsequently modify the quantum noise of the input field [18–20]. Two-photon bistability is also a well-known candidate for quantum-noise-reduction effects [11,15,21], and very intriguing predictions can also be made for the input-output transformation of the quantum noise of the two fields interacting in a two-photon double-beam optical system. Such a device therefore seems quite well suited for the study of quantum-noise effects and their relation with the associated mean-field instabilities.

ACKNOWLEDGMENTS

This work was supported by the European Economic Community under Contract No. ESPRIT BRA 3186 (“NOROS”).

- [1] (a) E. Abraham and S. D. Smith, *Rep. Pro. Phys.* **45**, 815 (1982); (b) L. A. Lugiato, in *Progress in Optics*, edited by E. Wolf (North-Holland, Amsterdam, 1984), Vol. XXI, p. 69; (c) H. M. Gibbs, *Optical Bistability: Controlling Light with Light* (Academic, New York, 1985).
- [2] F. T. Arecchi and A. Politi, *Lett. Nuovo Cimento* **23**, 65 (1978).
- [3] G. P. Agrawal and C. Flytzanis, *Phys. Rev. Lett.* **44**, 1058 (1980).
- [4] G. Grynberg, M. Devaud, C. Flyzantis, and B. Cagnac, *J. Phys. (Paris)* **41**, 931 (1980).
- [5] G. S. Agarwal, *Opt. Commun.* **35**, 149 (1980).
- [6] J. A. Hermann and B. V. Thompson, *Phys. Lett. A* **83**, 376 (1981).
- [7] E. Giacobino, M. Devaud, F. Biraben, and G. Grynberg, *Phys. Rev. Lett.* **45**, 434 (1980).
- [8] N. Peyghambarian, H. M. Gibbs, M. C. Rushford, and D. A. Weinberger, *Phys. Rev. Lett.* **51**, 1692 (1983); R. Levy, J. Y. Bigot, B. Honerlager, F. Tomasini, and J. B. Grun, *Opt. Commun.* **48**, 705 (1983).
- [9] A. K. Kar, J. G. H. Matthew, S. D. Smith, B. Davis, and W. Prettl, *Appl. Phys. Lett.* **42**, 334 (1983).
- [10] J. A. Hermann and D. F. Walls, *Phys. Rev. A* **26**, 2085 (1982).
- [11] P. Galatola, L. A. Lugiato, M. Vadicchino, and N. B. Abraham, *Opt. Commun.* **69**, 414 (1989).
- [12] L. M. Narducci, W. W. Edison, P. Furcinitti, and D.C. Eteson, *Phys. Rev. A* **16**, 1665 (1977).
- [13] B. Cagnac, G. Grynberg, and F. Biraben, *J. Phys. (Paris)* **34**, 845 (1973).
- [14] R. M. Whitley and C. R. Stroud, *Phys. Rev. A* **14**, 1498 (1976).
- [15] L. A. Lugiato, P. Galatola, and L. M. Narducci, *Opt. Commun.* **76**, 276 (1990).
- [16] P. Grangier and J. F. Roch, *Quantum Opt.* **1**, 17 (1989).
- [17] P. Grangier, J. F. Roch, and G. Roger, *Phys. Rev. Lett.* **66**, 1418 (1991).
- [18] M. G. Raizen, L. A. Orozco, M. Xiao, T. L. Boyd, and H. J. Kimble, *Phys. Rev. Lett.* **59**, 198 (1987).
- [19] S. Reynaud, C. Fabre, E. Giacobino, and A. Heidmann, *Phys. Rev. A* **40**, 1440 (1989).
- [20] F. Castelli, L. A. Lugiato, and M. Vadicchino, *Nuovo Cimento* **10D**, 183 (1988).
- [21] L. A. Lugiato and G. Strini, *Opt. Commun.* **41**, 374 (1982).

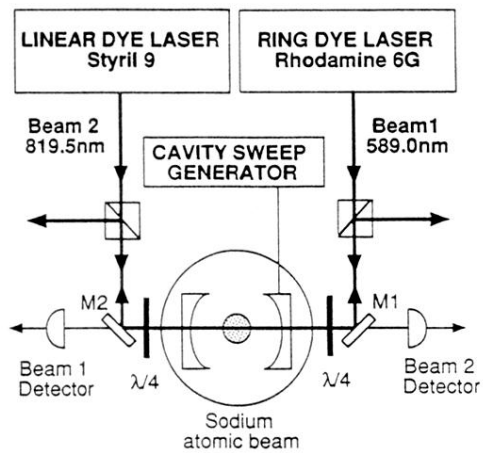


FIG. 1. Experimental setup. Two lasers at 589 and 819.5 nm are tuned close to resonances of the $3s_{1/2}$ - $3p_{3/2}$ - $3d_{5/2}$ cascade in a sodium atomic beam. The cavity resonates for each beam and is single-ended. The intracavity intensities are monitored through the dichroic mirrors M1 and M2.